Geophysical Journal International

Geophys. J. Int. (2014) **196,** 1525–1535
Advance Access publication 2014 January 16

doi: 10.1093/gji/ggt506

Volcanic hot spot detection from optical multispectral remote sensing data using artificial neural networks

Alessandro Piscini and Valerio Lombardo

Istituto Nazionale di Geofisica e Vulcanologia, Via di Vigna Murata 605 *Rome, Italy. E-mail: alessandro.piscini@ingv.it*

Accepted 2013 December 13. Received 2013 December 4; in original form 2013 July 22

SUMMARY

This paper describes an application of artificial neural networks for the recognition of volcanic lava flow hot spots using remote sensing data. Satellite remote sensing is a very effective and safe way to monitor volcanic eruptions in order to safeguard the environment and the people affected by such natural hazards. Neural networks are an effective and well-established technique for the classification of satellite images. In addition, once well trained, they prove to be very fast in the application stage.

In our study a back propagation neural network was used for the recognition of thermal anomalies affecting hot lava pixels. The network was trained using the three thermal channels of the Advanced Very High Resolution Radiometer (AVHRR) sensor as inputs and the corresponding values of heat flux, estimated using a two thermal component model, as reference outputs.

As a case study the volcano Etna (Eastern Sicily, Italy) was chosen, and in particular the effusive eruption which took place during the month of 2006 July. The neural network was trained with a time-series of 15 images (12 nighttime images and 3 daytime images) and validated on three independent data sets of AVHRR images of the same eruption and on two relative to an eruption occurred the following month.

While for both nighttime and daytime validation images the neural network identified the image pixels affected by hot lava with a 100 per cent success rate, for the daytime images also adjacent pixels were included, apparently not interested by lava flow. Despite these performance differences under different illumination conditions, the proposed method can be considered effective both in terms of classification accuracy and generalization capability. In particular our approach proved to be robust in the rejection of false positives, often corresponding to noisy or cloudy pixels, whose presence in multispectral images can often undermine the performance of traditional classification algorithms. Future work shall address application of the proposed method to data acquired with a high temporal resolution, such as those provided by the spinning enhanced visible and infrared imager sensor on board the Meteosat second generation geostationary satellite.

Key words: Image processing; Neural networks, fuzzy logic; Remote sensing of volcanoes.

1 INTRODUCTION

In the last 20 years, infrared (IR) remote sensing techniques for extracting volcanologically useful information have been used to study thermal structures of hot volcanic features such as lava flows, lava lakes, volcanic dome, pyroclastic flows and fumaroles (Rothery *et al*. 1988; Crisp & Baloga 1990b; Harris *et al.* 1999; Wright *et al.* 2000).

From the operational point of view, detection of new thermal anomalies, or of changes in existing ones, can be of special value for hazard assessment. Activity during effusive volcanic eruptions can change rapidly over periods of minutes to hours as new lava flows erupt or develop. The destructive potential of such phenomena makes timely information regarding their occurrence and development essential for hazard monitoring, assessment and response. Thus, satellite-based radiometers providing thermal data at high temporal resolution (>1 image per day) are suited to monitor effusive eruptions if timely analysed. These instruments provide data in which effusive events are easily detectable and changes in the style and extent of activity can be identified despite the coarse (1–25 km^2 pixel) spatial resolution of the data (e.g. Harris *et al.* 1997a,b; Wooster & Rothery 1997). Furthermore, these data can

be acquired directly at suitable receiving stations, processed within a few minutes and relayed to the agencies responible for volcanic hazard monitoring and assessment.

From the scientific point of view, remotely sensed thermal measurements can shed light into the physical processes that trigger eruptions and influence the behaviour of erupted materials, by providing estimates of the heat and mass fluxes of active lava flows. The movement of the latter is a complex subject that has provoked debate regarding the mechanisms that control the areal extent and physical character of the flow (e.g. Pieri & Baloga 1986; Lipman & Banks 1987; Oppenheimer 1991; Oppenheimer *et al.* 1993a,b,c; Harris *et al.* 1997a,b, 1998, 1999; Lombardo & Buongiorno 2006; Lombardo *et al.* 2006, 2009). Progress has been made in constructing useful mathematical models (e.g. Crisp & Baloga 1990; Pieri *et al.* 1990; Oppenheimer 1993b; Harris *et al.* 1997a,b, 1998, 1999; Lombardo *et al.* 2009). Determining volumetric effusion rates for lava flows from space is an important but challenging task. Effusion rates play a major role in evaluating flow dynamics and the potential threat posed by a lava flow. Higher effusion rates produce channel-fed flows that are longer, more rapidly moving, voluminous and more extensive than flows with low effusion rates (Walker 1973; Wadge 1977; Pieri & Baloga 1986). Flows with high effusion rates thus have far greater potential to inflict damage on distant communities with less advance warning. Measuring effusion rates is therefore of great interest. Field methods for their determinations are usually based on estimates of lava channel dimensions and lava flow velocity (e.g. Lipman & Banks 1987; Barberi *et al.* 1993). However, errors due to uncertainties in channel dimension, especially depth, are a major problem. Alternatively, if the eruption duration is known, accurate post-eruption measurements of total flow field volumes can provide reliable estimates of average effusion rates (e.g. Calvari *et al.* 1994). However, these averages will not reveal major variations in effusion rates which have been shown to occur during many basaltic eruptions (Wadge 1977).

Meteorological sensors have been increasingly employed for operational monitoring of volcanic thermal features. Satellite systems include the Eumetstat Meteosat second generation (MSG) spinning enhanced visible and infrared imager (SEVIRI; Ganci *et al.* 2011), the National Oceanic and Atmospheric Administration (NOAA) geostationary operational environmental satellites (GOES; Harris *et al.* 2001), the NASA moderate resolution imaging spectroradiometer (MODIS; Wright *et al.* 2004), the European Space Agency along track scanning radiometer (Colin *et al.* 2007) and the NOAA advanced very high resolution radiometer (AVHRR 2012; Webley *et al.* 2008; Marchese *et al.* 2011). The widely used AVHRR (2012) sensor provides a good compromise between spatial resolution and measurement frequency with the possibility of equipping volcanology institutes with a satellite receiving station (Harris *et al.* 1997b).

A different approach has been adopted for the identification of thermal activity using AVHRR data. The VAST algorithm has been developed by Harris, Higgins and Swabey (Harris *et al.* 1995, 2000b, 2002), the algorithm was later developed at the Hawai'i Institute of Geophysics and Planetology (HIGP) by Garbeil and Steffke (Steffke & Harris 2011). The algorithm is contextual, and uses the difference in brightness temperature between the mid (3.9 μm) and long-wave (10–12 μm) IR (ΔT). A region of interest (ROI) centred on the target volcano is extracted, and a threshold is taken from a region immediately surrounding the ROI in the same image. The threshold is the difference between the ΔT of the target pixel, and the mean of the eight pixels immediately surrounding the target. The maximum value from the background is taken as the threshold, and then any pixel within the ROI whose value exceeds the threshold is flagged as hot.

The robust satellite techniques identify hot spot detection (Pergola *et al.* 2004) computing a statistical index, in medium infrared (MIR) spectral band, using a multiyear time-series data of the same area.

AVHotRR is a robust routine for monitoring activity of volcanoes in the Mediterranean area (Lombardo *et al.* 2011). AVHotRR allows for automatic hot spot detection and effusion rate estimate of active lava flows using AVHRR and MODIS IR data. The AVHotRR routine is composed of graphical user-interface procedures that are implemented in Interactive Data Language (IDL) and takes advantage of the functionality of ENvironment for Visualizing Images (ENVI) for image managing/processing. The algorithm for 'hot spot detection' builds on the widely used 'dual-band' technique. Starting from the simultaneous solution of the Planck equation in two different IR bands, only a few combination of band radiances allow solutions of the dual-band problem. Not all of these solutions are physically acceptable, because not all of them satisfy the constraints of the two thermal component model assumed for active lava flows. The AVHotRR algorithm searches for pixels within the image which have solutions physically acceptable. If such pixels exist, they will be flagged as 'hot'.

Artificial neural networks (ANN) are relatively recent computational modelling tools, which have found wide acceptance in many disciplines due to their adaptability to complex real world problems (Rumelhart *et al.* 1995). The rapid diffusion of such neural approaches in remote sensing can be ascribed to their proven ability to learn complex models, taking into account any non-linear relationships between the explanatory and dependent variables (Lek & Guegan 1999). ANN approaches are suitable for the analysis of different data types (Civco 1993; Benediktsson & Sveinsson 1997; Carpenter *et al.* 1997) and can be generalized to noisy environments, which allows for robust solutions even in the presence of incomplete or inaccurate data (Hewitson & Crane 1994). Furthermore, *a priori* knowledge of physical constraints as well as ancillary data are not required (Foody 1995a,b).

ANN can be defined as a structure composed of densely interconnected simple adaptive processing elements (called artificial neurons or nodes), capable of performing calculations for massively parallel processing of data and knowledge representation (Hecht-Nielsen 1990; Schalkoff 1997).

ANN learning is performed iteratively as the network is presented with training examples, similar to the way we learn from experience. An ANN-based system is said to have learnt if it can (i) handle imprecise, fuzzy, noisy and probabilistic information without noticeable adverse effect on response quality, and (ii) generalize from the tasks it has learned to unknown ones.

An additional advantage of the ANN approach is that ANNs can perform supervised classification using fewer training data than those with maximum probability, because rules of recognition of a given category are based on the attributes, not only of training data of that particular category class, but also of other classes (Paola & Schowengerdt 1995).

It was reported that ANNs have more accurate performance than other techniques such as statistical classifiers, especially when the functional space is particularly complex and the source of data presents different statistical distributions (Benediktsson *et al.* 1990, 1993; Schalkoff 1992).

Concerning applications of ANNs to natural hazard monitoring and in particular to thermal anomalies recognition, many studies have been carried out to map wildfires and forest damages. ANNs were used for classifying forest damages from Landsat Thematic Mapper data (Ardo *et al.* 1997). A study was conducted by Al-Rawi *et al.* (2001) to build a multitemporal multispectral automatic burned area mapping system and fire detection system. Detection of fire smokes was carried out using AVHRR imagery (Li *et al.* 2001) and ANN was compared to the conventional classification methodology in forest fire analysis (Sunar & Ozkan 2001).

To date no significant studies involving volcanic lava flow monitoring using ANNs have been carried out. The main objective of this study is to verify if such a technique may be useful and give substantial improvements for real time monitoring of lava flow hot spots, overcoming the drawbacks of traditional classification algorithms, like false alarm detection due to noisy or cloudy pixels.

From the perspective of pattern recognition, neural networks can be regarded as an extension of the many conventional statistical techniques which have been developed over several decades (Bishop 1995). More extensive treatments of these topics can be found in the many text books on statistical pattern recognition, including Duda & Hart (1973), Hand (1981), Devijver & Kittler (1982), and Fukunaga (1990). Review articles by Ripley (1994) and Cheng & Titterington (1994) have also emphasized the statistical underpinnings of neural networks.

The main tasks of remote sensing data analysis in which the application of ANNs is reported are classification, more commonly land cover classification, namely the process in which pixels are grouped according to the similarities of their spectral properties. If a pixel satisfies a certain set of criteria then it is assigned to the land cover class that corresponds to those criteria. This is the most common task achieved with remote sensing, and applications that involve both supervised and unsupervised ANNs are numerous. Due to the absence of assumption about the data, many land cover classifications use data from different sensors such as optical and radar images (Benediktsson & Sveinsson 1997; Augusteijn & Warrender 1998), texture and ancillary data. Texture is incorporated in different ways: (i) precomputed per pixel texture information that is fed to the ANN together with the spectral information (Lloyd *et al.* 2004) or (ii) incorporating neighbouring spectral information using a sliding window (Kurnaz *et al.* 2005).

The most currently used ancillary information are topographic variables derived from a digital elevation model (Bischof *et al.* 1992; Dreyer 1993; Kaminsky *et al.* 1997; Kontoes *et al.* 2000; Lloyd *et al.* 2004; Tatem *et al.* 2004; Keramitsoglou *et al.* 2005; Kurnaz *et al.* 2005). Other variables are the coordinates (latitude/longitude; Carpenter *et al.* 1999) and distance to coast and soil (Mas 2004). Some attempts have been made to develop classifiers based on the synergism between ANNs and knowledge-based systems (Murai & Omatu 1997; Qiu & Jensen 2004).

2 DATA AND METHODS

The neural network must first be 'trained' by having it process a large number of input patterns and their associated reference output patterns. Once trained, the neural network is able to recognize similarities when presented with a new input pattern, resulting in a predicted output pattern. Therefore, an AVHRR data set has been chosen at first attempt, since it provides a good compromise between high spatial resolution (e.g. ASTER, Landast series) and high temporal resolution data (e.g. GOES and MSG). AVHRR was also preferred over the MODIS sensor (similar spatial resolution but better radiometry) because of the larger number of images available for our study case (the 2006 Etna eruption).

Table 1. AVHRR spectral sensor characteristics.

AVHRR	NOAA 12, 14 (μm)	NOAA 15, 16, 17, 18, 19 (μm)
Channel 1 (VIS)	0.58–0.68	0.58–0.68
Channel 2 (NIR)	0.725–1.1	0.725–1.1
Channel 3A (MIR)	3.55–3.9	3.55–3.9
Channel 3B (MIR)	–	1.58–1.64
Channel 4 (TIR)	10.3–11.3	10.3–11.3
Channel 5 (TIR)	11.4–12.4	11.4–12.4

2.1 AVHRR data

The AVHRR aboard the NOAA polar orbiting satellites is a multispectral sensor that acquires radiance images in the wavelength range from visible (VIS) to thermal infrared (TIR; 0.6–12.5 μm). The first AVHRR, launched on Television and Infra-Red Observation Satellite-N (TIROS-N) in October 1978, was a four-channel radiometer. It was subsequently upgraded to a five-channel instrument (AVHRR-2), initially carried on NOAA-7, launched in 1981 June.

The latest instrument version is AVHRR-3, with six channels, first carried on NOAA-15, launched in May 1998. With an orbit altitude of about 833 km and a scanning angle of $\pm 55.3^{\circ}$, the total swath width is about 2900 km. The spatial resolution at nadir is 1.1 km and increases to about 5 km at the most extreme off-nadir viewing angles. The AVHRR-3 carries two visible near IR channels with bandpass wavelengths (bandwidths) of 0.58–0.68 μm and 0.725–1.1 μm, two time-shared channels, centred around 1.6 μm for daytime images and around 3.75 μm for nighttime images, and two channels in the TIR spectral region with bandwidths of 10.3–11.3 and 11.5–12.5 μm (Davis 2007; AVHRR 2012, see Table 1).

2.2 Hot spot detection

The procedure by Lombardo *et al.* (2004, 2011) allows automatic hot spot detection and estimation of lava flow total thermal flux and effusion rate during volcanic crisis phases.

A first step consists of detection of cloudy pixels that will be excluded from thermal flux computation. A determination of the presence of global cloudiness is essential to volcanic monitoring for two reasons: first, clouds play a critical role in hot spot detection and must be accurately described to allow thermal anomaly identification; secondly, the presence of cloudiness must be accurately determined to correctly retrieve the radiant contribution from potential thermal anomalies. For many retrieval algorithms even thin cirrus clouds are an issue. The cloud detection model proposed by Chen *et al.* (2002) has been implemented for daytime images while a modified version of the algorithm developed by Spangenberg *et al.* (2002) has been used for nighttime images. Such algorithms have been adapted to Mt Etna's seasonal conditions (e.g. accounting for snow in winter time).

The algorithm searches for pixels that satisfy the two thermal component model using the dual-band technique. Very hot volcanic surfaces, such as lava flows, lakes and domes, magma-filled conduits and fumaroles vents, often present temperature variations of hundreds of degrees over spatial scales of only a few centimetres

(Oppenheimer *et al.* 1993a). Thus, the 'footprint' of remote sensing instruments comprising such features (from space borne or airborne platforms) typically encompasses highly inhomogeneous radiant temperature patterns.

Pixel dimensions of satellite data (1–3 km) often exceed the width of lava bodies. Therefore, we consider a two thermal component model in which a hot component refers to the lava integrated temperature and occupies a pixel fraction f_{lava}, and a cooler component models the contribution of the surrounding background temperature (T_b), which occupies a pixel fraction f_b.

An automatic 'hot spot detection' procedure, which uses the mathematical and physical relationships derived by the theoretical solution of the 'dual band' system of equations and a digital filter to single out hot radiant pixels, has been proposed by Lombardo *et al.* (2004), using Landsat TM short wave infrared (SWIR) bands. The filter was initially developed for detection of volcanic hot spots and then adapted to allow the detection of different thermal anomalies including active lava flows. This algorithm has been adapted to AVHRR band 3 (MIR) and 4 (TIR) assuming a two thermal component model for active lava flows. The first part of the filter builds on the assumption that fractional area f_{lava} must be greater than zero. The second part of the filter verifies the condition that subpixel lava T_{lava} temperature must be greater than 0 °C (Lombardo *et al.* 2011).

2.3 Dual-band technique using a two thermal component model

We can solve the system using one SWIR/MIR band to characterize the hottest component lava body (T_{lava}) and one TIR band (8–12 μm) for cooler background (T_b). This is the so called dual-band technique applied to a two-thermal component model using low spatial resolution data (Harris *et al.* 1997a).

Usually, this technique allows the estimation of T_{lava} and f_{lava} if T_b is assumed. It is possible to estimate the background temperature from the non-radiant pixels surrounding the lava body if the background emissivity is known. However, lava pixels that are adjacent to cloudy or noisy pixels are likely to generate incorrect ambient temperatures leading to either positive or negative false alarms (Oppenheimer 1991; Donegan & Flynn 2004; Blackett & Wooster 2011; Lombardo *et al*. 2011).

The retrieved subpixel lava temperature will be of course an average value between crust and molten lava temperatures.

The subpixel temperature retrieval technique is pivotal in remote-sensing of active lava flows. The algorithm uses the globally convergent Broyden's method to solve the dual-band equation system:

$$L(T_x\lambda_3) = \varepsilon_3\tau_3\left[f_1 L(T_1\lambda_3) + (1 - f_1)L(T_b\lambda_3)\right], \quad (1)$$

$$L(T_y\lambda_4) = \varepsilon_4\tau_4\left[f_1 L(T_1\lambda_4) + (1 - f_1)L(T_b\lambda_4)\right], \quad (2)$$

where L is the Planck function for a black body radiating to temperature T and wavelength λ, T_x and T_y are the pixel integrated temperatures in AVHRR bands 3 and 4, respectively, ϵ is spectral emissivity and τ is atmospheric trasmissivity (Wan & Dozier 1989).

A quite uniform surface of basaltic lavas characterize Mt Etna's summit area. Therefore, T_b can be estimated assuming a suitable ϵ for Etnean cold basalts. Because T_b may vary widely from vent to flow toe, the procedure retrieves the maximum (T_{bmax}) and minimum temperature (T_{bmin}) of the background in a pixel mask surrounding the thermal anomaly. Dual-band solutions (T_{lava} and f_{lava}) are then calculated for every T_b between T_{bmin} and T_{bmax}. The dual-band approach requires knowledge of the values of one of the three unknowns: lava temperature (T_{lava}), background temperature (T_b) and fraction of pixel occupied by lava (f_{lava}).

AVHotRR derives T_b from non-active pixels surrounding the thermal anomaly, under the assumption of known background emissivity (Lombardo *et al.* 2011).

2.4 Estimating the energy flux radiated by an active lava flow

The energy produced by an active lava flow is transferred to the environment through a combination of conduction, convection and radiation. Thermal IR remote sensing research has focused on inferring information from the radiative component, as the convective and conductive components are difficult to quantify directly. The radiative transfer underlying an observed lava flow scene is very complex: in the same area there are zones not yet touched by the lava flow, burning zones and zones already burnt; in the burning zones at least two distinct lava flow stages, flaming and smoldering, are to be considered, characterized by different temperatures, and emission rates.

Moreover, the atmospheric loading is very complex too, with the presence of ash and hot smoke and increased water vapour content.

In general the retrieval of lava parameters from space is based on a simplified RTM, often referred to as Dozier Model (Dozier 1981).

In this approach a burning pixel is seen as a 'mesoscale' composite target made up of two 'grey' body targets linearly combined through coefficients representing the fractions of the burning and non-burning portions of the pixel. Of course this model restricts the observation of the active lava flow to the TIR emission bands. Nevertheless, according to the Wien displacement law the peak of the surface emitted radiance shifts to shorter wavelengths as the surface temperature increases so that temperatures of about 1000 K can give significant signal contribution in the SWIR region, where emission and reflection phenomena compete, so that a more complex RTM is needed to interpret the data.

Following Oppenheimer (1991) and Harris *et al.* (1997a,b, 1998, 2000a) we derive the total flux Q_{tot} assuming that heat loss can be described by a simple model for a subaerial channel-fed flow where:

$$Q_{tot} = Q_{rad} + Q_{conv} + Q_{cond}. \quad (3)$$

Q_{rad}, Q_{conv} and Q_{cond} are the total radiant heat flux, the convective heat and the conducted heat fluxes, respectively. Q_{rad} for each pixel containing active lava ($Q_{rad}(p)$) is calculated using:

$$Q_{rad}(p) = \varepsilon\ \sigma\ A_p[f_{lava}T_{lava4} + (1 - f_{lava})T_{b4}], \quad (4)$$

in which ϵ is the emissivity, σ is the Stefan-Boltzmann constant (5.67×10^{-8} W m^{-2} K^{-4}) and A_p is the AVHRR pixel area. An emissivity of 0.98 was chosen to be representative of Etnean lava flows (Buongiorno *et al*. 1999, 2002). Total radiative heat loss is then obtained by summing $Q_{rad}(p)$ for every lava pixel. Q_{conv} is estimated for the entire lava flow field in a similar way, where Q_{conv} for each pixel of the image containing active lava ($Q_{conv}(p)$) is calculated using the free convection case given by Harris *et al.* (1997b, 1998). This reduces to:

$$Q_{conv}(p) = h_c[T_{surf} - T_{air}], \quad (5)$$

in which h_c is the convective heat transfer coefficient, T_{surf} is the lava surface temperature, and T_{air} is the ambient air temperature, where the values given in Harris *et al*. (1997b) result in values for h_c of 5–12 W m^{-2} K^{-1} for free convection. This is a theoretically calculated value for free convection (see Harris *et al.* 2005), whereas

values for forced convection obtained from measurements (Keszthelyi *et al.* 2003) and modelling (Patrick *et al.* 2005) indicate higher values ($\sim$50 W m^{-2} K^{-1}). The heat conducted through the base of the flow is given by (Harris *et al.* 1997b):

$$Q_{\rm cond} = Ap\ k\ \delta T/\delta h. \quad (6)$$

where $k = 2.5 - 3.2$ W m^{-1} K^{-1}, $\delta T = 520$ K (assuming core temperature of 1100 °C and a basal contact temperature of 580 °C) and $\delta h = 0.2$ m (hot model) or 3.0 m (cold model). This can account for $\sim$25 per cent of the total heat loss ($Q_{\rm tot}$). In reality the assumptions involved mean that the main variable is active lava area ($A_{\rm lava}$), so that the above steps define the slope of a linear relationship between effusion rate and lava flow area (Wright *et al.* 2001).

2.5 Neural network methodology

ANNs are based on the concept of the single artificial neuron, the 'perceptron' introduced by Rosenblatt in 1958 (Rosenblatt 1962) to solve problems in the field of character recognition (Hecht-Nielsen 1990). An artificial processing neuron receives inputs as stimuli from the environment, combines them in a special way to form a 'net' input, which is then filtered through a linear threshold gate. The output signal is forwarded to another neuron or to the environment. Only when the 'net input' exceeds the neuron's threshold limit (also called bias), will the neuron become activated. The activation at that node is calculated using a transfer function (e.g. sigmoidal function) to yield an output between 0 and 1 or -1 and $+1$. The amount of activation obtained represents the new signal that is to be forwarded to the subsequent layer (e.g. either hidden or output layer). The same procedure of calculating the net effect is repeated for each hidden node and for all hidden layers (Bishop 1995). The perceptron can be trained on a set of examples using a special learning rule (Hecht-Nielsen 1990). The perceptron weights (including the threshold) are changed according to the difference (error) between the target (correct) output, Y, and the perceptron solution, y, for each example.

The error is a function of all the weights and forms an irregular multidimensional complex hyper plane with many peaks, saddle points and minima. Using a specialized search technique, the learning process seeks to obtain the set of weights that corresponds to the global minimum. One of these is the backpropagation algorithm, which consists of two phases: in the feed-forward pass, an input vector is presented to the network and propagated forward to the output; in the backpropagation phase, the network output is compared to the desired output; network weights are then adjusted in accordance with an error-correction rule. Hence the name 'back-propagation' Rumelhart *et al.* (1986), Bishop (1995) or Haykin (1999).

The performance of a trained ANN is generally assessed by computing the root mean squared error between the expected values and the activation values at the output nodes or, in the case of classification, the percentage of correctly classified examples of the validation set.

In order to cope with non-linearly separable problems, additional layer(s) of neurons placed between the input layer (containing the input nodes) and the output neuron are needed leading to the multilayer perceptron (MLP) architecture (Hecht-Nielsen 1990).

In this work, backpropagation neural networks (BPNN) have been used. These networks are the most widely used type for their flexibility and adaptability in modelling a wide spectrum of problems in many application areas (Rumelhart *et al.* 1986). A BPNN is an MLP consisting of an input layer with nodes representing input variables to the problem, an output layer with nodes representing the dependent variables (i.e. what is being modelled), and one or more hidden layers containing nodes to capture the non-linearity in the data. Using supervised learning, with the error-correction learning rule for network weights adjustments, these networks can learn the mapping from one data space to another using examples. The term backpropagation refers to the way the error computed at the output side is propagated backward from the output layer, to the hidden layer, and finally to the input layer. In BPNNs, the data are fed forward into the network without feedback (i.e. all links are unidirectional and there are no same layer neuron-to-neuron connections). The neurons in BPNNs can be fully or partially interconnected. These networks are so versatile and can be used for data modelling, classification, forecasting, control, data and image compression, and pattern recognition (Hassoun 1995).

A neural network for lava flow hot spot detection was implemented using a training set of 15 AVHRR images, of which 12 nighttime and 3 daytime images, respectively, spanning the 2006 July Mt Etna eruption (Sicily, Italy). Estimation of thermal flux using the methods by Lombardo *et al.* (2004, 2011) was carried out on these images to flag pixels affected by lava flow and generate a target output data set.

The total training samples were 14 415 of which 149 were classified as hot spots, based on thermal flux estimation. The network topology consists of three inputs, namely the brightness temperatures in the AVHRR thermal channels, centred around 3.9, 11 and 12 μm, comprising the range of wavelengths containing information used for thermal flux estimation. Ten neurons were used in a single hidden layer. Finally, two network outputs correspond to the two possible classification results, namely 'hot spot' and 'non-hot spot'.

When training a neural network, it is of interest to obtain a network with an optimal generalization performance, that is the network performance should not degrade significantly when data sets other than the training one are analysed.

Standard neural network architectures, like the fully connected multi layer perceptron, have almost always a too large parameter space, and are prone to over-fitting (Geman *et al.* 1992). During the training phase, although the network performance appears to constantly improve on the training sets, at some point it actually begins to worsen in terms of errors on unseen data sets. Cross validation can be used to detect when over-fitting starts, during supervised training of the neural network; training can then stopped before convergence to avoid over-fitting, a process called early stopping (Prechelt 1998).

In this study, early stopping was carried out by splitting the training data into three sets: a training one, a cross-validation one and a test one. These consisted, respectively, of 60 , 30 and 10 per cent of the total number of training samples. The first set was used for network training. The cross-validation set was analysed at a predefined number of epochs, to assess performance on a data set other than the training one. The training was stopped after the error calculated on the cross-validation set was greater than that of the training one for six consecutive iterations. Finally, the test set was used during the training phase as an independent data source to assess network performance.

After completion of the training process, validation of the network was carried out on an independent data set, not used during the training, consisting of three AVHRR images acquired in 2006 July and two in 2006 August. Concerning the hidden layer's size, typically a single hidden layer is sufficient to approximate continuous functions (Hecht-Nielsen 1990; Basheer 2000). Two hidden layers may be necessary for functions with discontinuities (Masters 1994).

The determination of the appropriate number of hidden layers and number of hidden nodes (NHN) in each layer is one of the most critical tasks in ANN design. Unlike the input and output layers, one starts with no prior knowledge as to the number and size of hidden layers. As the NHN increases, training becomes excessively time-consuming.

The optimal NHN essential for network generalization is in general a function of the input/output vector sizes, the size of the training and test subsets and, more importantly, the underlying non-linearity of the observed phenomena. Several rules of thumb are available in the literature, which relate hidden layer size to the number of input nodes (N_{INP}) and output layers (N_{OUT}). Jadid & Fairbairn (1996) called for an upper bound on NHN equal to NTRN/[R + (N_{INP} + N_{OUT})], where NTRN is the number of training patterns and $R = 10$. Using this equation we obtain an NHN of 961. Instead Masters (1994) suggested that the NN architecture should resemble a pyramid with NHN circa $(N_{INP} * N_{OUT})^{1/2}$, providing in our case an NHN of 2.5. Given this huge range of variation, we decided not to rely on theory alone, and to begin with a number of three hidden nodes, building on as needed to meet the model accuracy demand. Our final choice of a single hidden layer of ten nodes was found to provide the best accuracy.

3 THE TEST CASE AND STUDY RESULTS

3.1 Test case description: Etna eruptions 2006 July–September

On 2006 July 14, a fissure opened on the East flank of the South East Crater of Etna and produced a lava flow that travelled East to the Valle del Bove. Moderate Strombolian activity from the East flank of the South East Crater produced a small amount of ash fall on Catania (∼25 km South South East of the volcano). The lava flow reached a maximum distance of 3 km within the Valle del Bove and ceased on July 24. On July 26, strong explosions were heard from the rim of the North East crater.

On August 31, Strombolian activity from the summit of the SE Crater produced lapilli and bombs that fell mainly in the crater. The ejecta filled the crater and overflowed on the E side on September 5, forming lava falls that accumulated in a steep-sided circular depression on the middle part of the E flank. On September 7, the sluggish 'A' ā flow breached the E rim and spread out on the E flank of the SE Crater and towards the Valle del Bove rim. Explosive activity at the SE Crater summit produced lava blocks that fell to the base of the cone.

On September 10, a rockfall from a wall that divided the SE Crater and the depression on the middle part of the E flank produced an ash plume that drifted W. Lava flows and Strombolian activity from the summit of the SE Crater continued on September 11 (Smithsonian Institution, Global Volcanism Program 2013).

3.2 Results and discussion

In order to evaluate the performance of neural networks in terms of their generalization capability and accuracy in detecting lava flow hot spots, we applied the trained neural network classifier to a validation set consisting of three independent AVHRR images belonging to the 2006 July Etna eruption and to two independent AVHRR images belonging to the following event, occurred on 2006 August.

Table 2. Confusion matrix assessing the classification accuracy on a test of 10 per cent of the AVHRR training samples.

Test Set 10 per cent		Hot spot		User acc.
Accuracy: 100 per cent		Yes	No	(per cent)
NN	Yes	15	0	100
	No	0	1427	100

Table 3. Confusion matrix assessing the classification accuracy on the AVHRR validation set of 2006 July 20, 16:05 UTC.

2006 July 20, 16:05 UTC.		Hot spot		User acc.
Accuracy: 99.8 per cent		Yes	No	(per cent)
NN	Yes	3	2	60
	No	0	956	100

Performance was assessed in terms of overall accuracy and user accuracy. The former represents the percentage of correct classifications, with respect to the total number of pixels analysed, considering all classes (i.e. 'hot spot' and 'non-hot spot'). The user accuracy instead represents the percentage of correct classifications for each network output class.

Table 2 shows the result obtained processing the training test data set (10 per cent of the total training samples). The overall and user accuracy are 100 per cent, without omission (false negatives) or commission (false positive) errors.

Tables 3–7 describe the confusion matrices obtained applying the NN classifier to the five images constituting the validation data set. Figs 1–5 show comparisons between classification maps obtained from the NN classifier and from the hot spot detection algorithm for all validation data sets.

In Tables 4 and 5, which summarize the results related, respectively, to the 2006 July 24, 04:31 UTC and 2006 July 28, 04:53 UTC images, the neural network classifier once again achieves an accuracy level of 100 per cent. This is a very good result, considering that the latter image contains many noisy pixels as shown on Fig. 6 (bottom-left).

Table 6 shows the confusion matrix computed applying the NN classifier to the 2006 August 14, 20:30 UTC AVHRR image. Despite the presence of false alarms (noise) in some image pixels clearly evident in the MIR and TIR images depicted in Fig. 4 (top, left and

Table 4. Confusion matrix assessing the classification accuracy on the AVHRR validation set of 2006 July 24, 04:31 UTC.

2006 July 24, 4:31 UTC.		Hot spot		User acc.
Accuracy: 100 per cent		Yes	No	(per cent)
NN	Yes	4	0	100
	No	0	957	100

Table 5. Confusion matrix assessing the classification accuracy on the AVHRR validation set of 2006 July 28, 04:53 UTC.

2006 July 28 4:53 UTC.		Hot spot		User acc.
Accuracy: 100 per cent		Yes	No	(per cent)
NN	Yes	1	0	100
	No	0	960	100

Table 6. Confusion matrix assessing the classification accuracy on the AVHRR validation set of 2006 August 14, 20:30 UTC.

2006 August 14, 20:30 UTC.		Hot spot		User acc.
Accuracy: 100 per cent		Yes	No	(per cent)
NN	Yes	1	0	100
	No	0	960	100

Table 7. Confusion matrix assessing the classification accuracy on the AVHRR validation set of 2006 August 31, 20:39 UTC.

2006 August 31, 20:39 UTC.		Hot spot		User acc.
Accuracy: 99.9 per cent		Yes	No	(per cent)
NN	Yes	1	1	50
	No	0	959	100

right), the pixels classified as hot spots are indeed such, that is there are no false detections.

Table 7 shows the confusion matrix of the NN classifier applied to the 2006 August 31, 20:39 UTC AVHRR image. The classifier detects pixels affected by lava, despite the clouds affecting many image pixels (see Fig. 6, bottom-right). User accuracy is 50 per cent because the classifier detects one more pixel. For the latter, a thermal flux estimate could not be produced, that is the thermal flux model output is a NaN, meaning that validation is lacking for this pixel. Another reason might be due illumination conditions, because nighttime images were not well represented by training data sets (only 20 per cent).

The last two cases are very significant concerning network performance in the presence of cloudy or noisy image pixels.

The most interesting case is represented by the 2006 July 20, 16:05 UTC daytime image. Table 3 shows the confusion matrix obtained and indicates an overall accuracy of 99.8 per cent. This is due to the presence of a commission error, which determines the

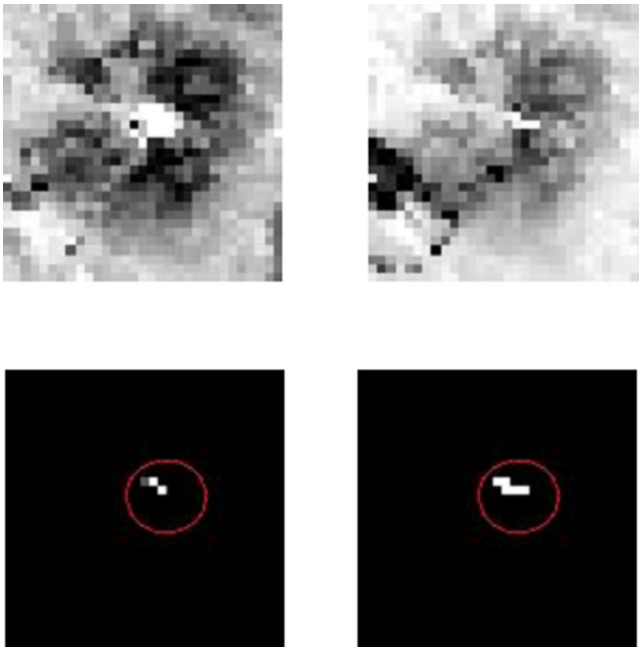

Figure 1. 2006 July 20, 16:05 UTC validation set. Top: AVHRR image in MIR band (left), TIR band (right). Bottom: Lava hot spot (left), hot spot detected by neural network classifier (right).

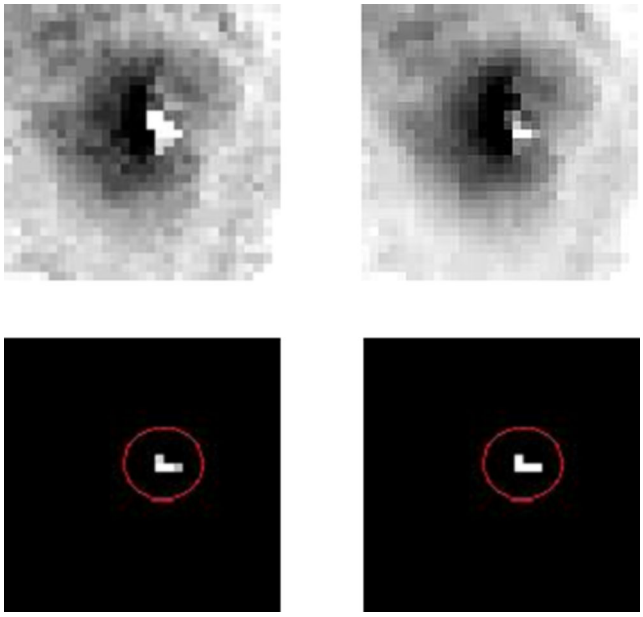

Figure 2. 2006 July 24, 4:31 UTC validation set. Top: AVHRR image in MIR band (left), TIR band (right). Bottom: Lava hot spot (left), hot spot detected by neural network classifier (right).

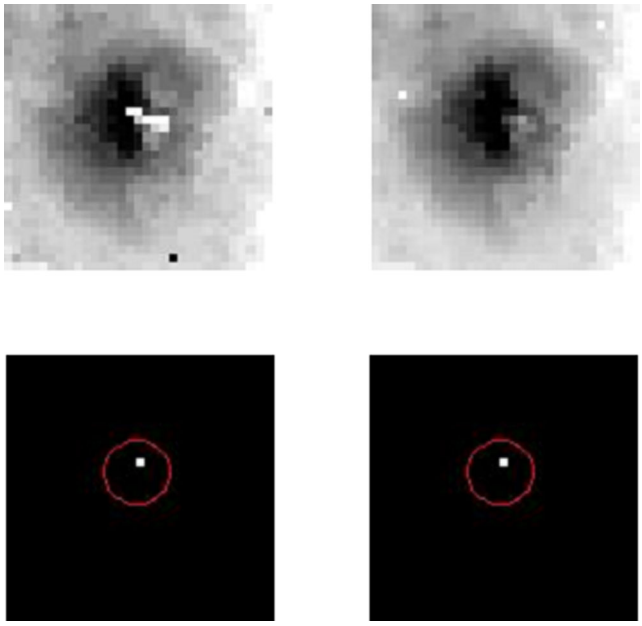

Figure 3. 2006 July 28, 4:53 UTC validation set. Top: AVHRR image in MIR band (left), TIR band (right). Bottom: Lava hot spot (left), hot spot detected by neural network classifier (right).

user accuracy value of 60 per cent. The neural network classifier did not make any omission error, correctly classifying all hot lava pixels, but detected two spurious pixels (commission errors). Fig. 1 (bottom-right), shows that these two pixels are close to other three correctly classified hot spot pixels.

Analysis of AVHRR data highlighted the presence of cloudy pixels in the proximity of lava hot spots (Fig. 6, top-left). In fact, temperatures of two pixel detected in MIR are similar to the middle pixel, while temperature in channel 4 (TIR) is lower than 30 °C, a significant difference from the middle pixel, showing a temperature in channel 4 of 62 °C. Using background temperatures derived from

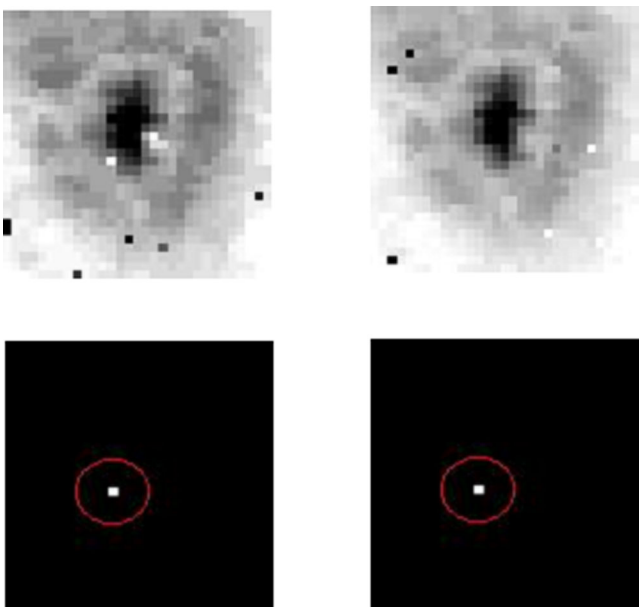

Figure 4. 2006 August 14, 20:30 UTC validation set. Top: AVHRR image in MIR band (left), TIR band (right). Bottom: Lava hot spot (left), hot spot detected by neural network classifier (right).

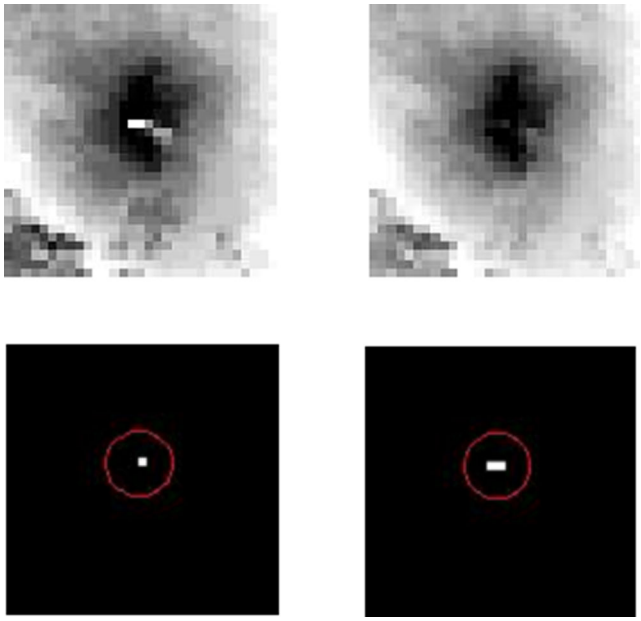

Figure 5. 2006 August 31, 20:39 UTC validation set. Top: AVHRR image in MIR band (left), TIR band (right). Bottom: Lava hot spot (left), hot spot detected by neural network classifier (right).

these pixels in the system of eq. (1) non-acceptable solutions are obtained. The AVHotRR algorithm was then implemented to verify the accuracy of dual-band results and to reject pixels associated with unacceptable solutions.

This latter case reveals a false negative because the pixel is affected by lava but it is not considered in the thermal flux computing, and the neural network classifier reveals its effectiveness in hot spot detection with high accuracy.

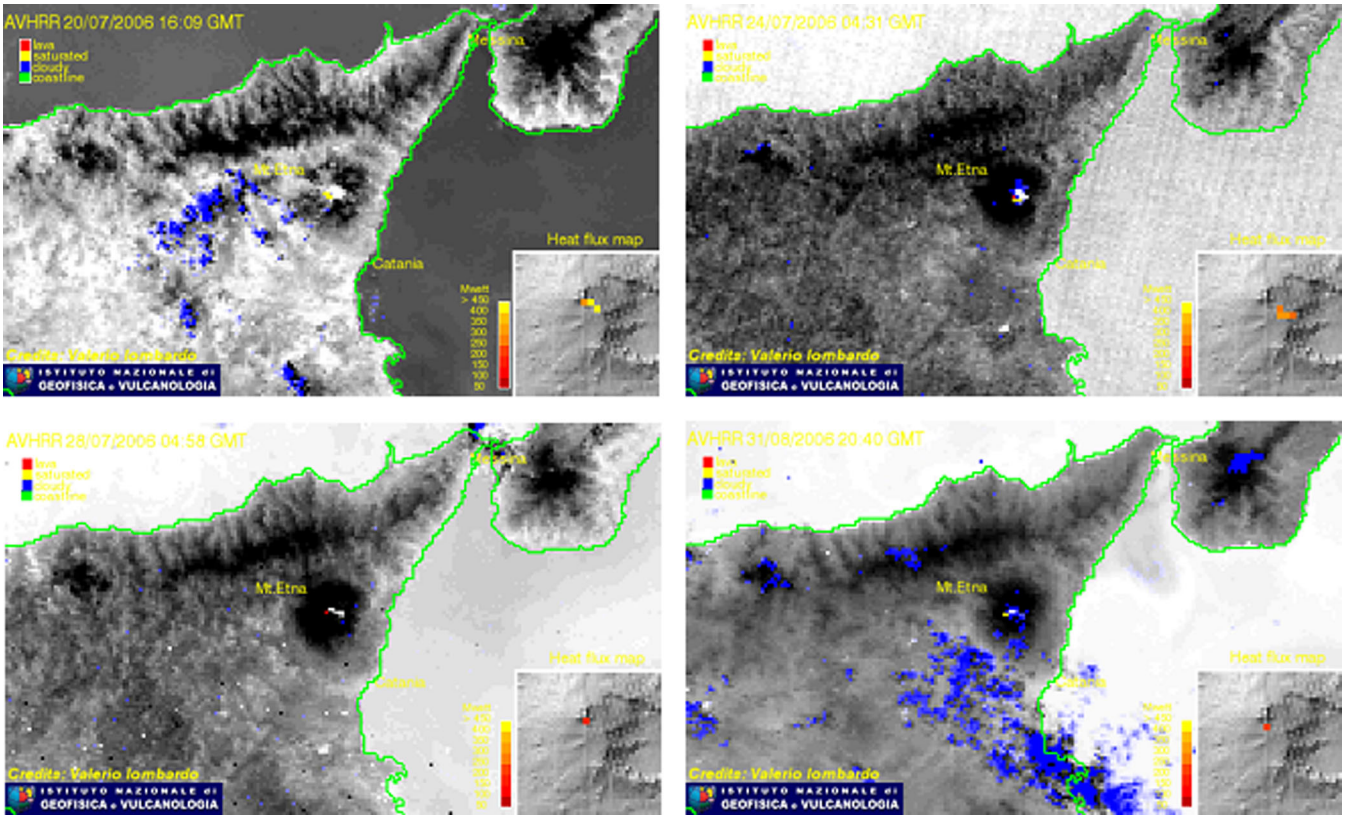

Figure 6. Classification of AVHRR images. Top left: 2006 July 20, 16:05 UTC. Top right: 2006 July 24, 4:31 UTC. Bottom left: 2006 July 28, 4:53 UTC. Bottom right: 2006 August 31, 20:39 UTC. In red, lava pixels. In yellow, colour saturated pixels.

4 CONCLUSIONS

This work proves the detection capability of lava hot spots by means of a neural network classifier, applied to the thermal channels of the AVHRR sensor. Lava flow thermal flux estimations were used as training target outputs. The classifier works well both on daytime and nighttime images.

The resulting confusion matrices associated with the classifier's application to independent data sets spanning two Etna volcanic eruptions revealed an accuracy of 100 per cent on 60 per cent of tested images. On the remaining 40 per cent, detection accuracy was slightly lower, but these cases included:

(1) The validation data set was a daytime image that represented only 20 per cent of the AVHRR time-series training samples.

(2) Likelihood of the presence of false negatives, that is pixels affected by hot lava flow but not included in thermal flux estimations. In this case thermal analysis is needed in order to establish if the classifier generated false negatives or false positives.

Nevertheless the neural network classifier successfully overcame the detection of false positives present in the validation data set images, like noisy or cloudy pixels, whose presence in multispectral images can often undermine the performance of traditional classification algorithms. Therefore, the proposed method represents a reliable new approach for volcanic hot spot detection and due to its fast application in the operational stage it demonstrates also its usefulness in near real time volcanic monitoring activities.

Future activities include the construction of a classifier able to exploit the fine timing resolution provided by other sensors, such as SEVIRI on board MSG geostationary satellite or NASA-USGS Landsat 8. We also plan to apply the ANN approach to detect volcanic hot spots from MODIS data. To better assess the operational performance, our results will be discussed in comparison with those obtained by MODVOLC, a well-established, MODIS-based algorithm for hot spot detection that is used worldwide.

ACKNOWLEDGEMENTS

The authors would like to thank John Peter Merryman Boncori for carefully reading the original manuscript and for providing language corrections. Special thanks go to Klemen Zaksek and to an anonymous reviewer, whose comments significantly improved the paper.

REFERENCES

Al-rawi, K.R., Casanova, J.L. & Calle, A., 2001. Burned area mapping system and fire detection system, based on neural networks and NOAA-AVHRR imagery, *Int. J. Remote Sens.,* **22,** 2015–2032.

Ardo, J., Pilesjo, P. & Skidmore, A., 1997. Neural networks, multitemporal Landsat Thematic Mapper data and topographic data to classify forest damages in the Czech Republic, *Can. J. Remote Sens.,* **23,** 217–229.

Augusteijn, M.F. & Warrender, C.E., 1998. Wetland classification using optical and radar data and neural network classification, *Int. J. Remote Sens.,* **19,** 1545–1560.

AVHRR (Advanced Very High Resolution Radiometer), 2012. *NOAA Satellite and Information Service*. Available at: http://noaasis.noaa.gov/NOAASIS/ml/avhrr.html (last accessed 4 December 2012).

Barberi, F., Rosi, M. & Sodi, A., 1993. Volcanic hazard assessment at Stromboli based on review of historical data, *Acta Vulcano.,* **3,** 173–187.

Basheer, I., 2000. Selection of methodology for modeling hysteresis behavior of soils using neural networks, *J. Comput.-Aided Civil Infrastruct. Eng.* **5**(6), 445–463.

Benediktsson, J.A. & Sveinsson, J.R., 1997. Feature extraction for multisource data classification with artificial neural networks, *Int. J. Remote Sens.,* **18,** 727–740.

Benediktsson, J.A., Swain, P.H. & Ersoy, O.K., 1990. Neural network approaches versus statistical methods in classification of multisource remote sensing data, *IEEE Trans. Geosci. Remote Sens.,* **28,** 540–551.

Benediktsson, J.A., Swain, P.H. & Ersoy, O.K., 1993. Conjugate gradient neural networks in classification of multisource and very high dimensional remote sensing data, *Int. J. Remote Sens.,* **14,** 2883–2903.

Bischof, H., Schneider, W. & Pinz, A.J., 1992. Multispectral classification of Landsat-images using neural networks, *IEEE Trans. Geosci. Remote Sens.,* **30,** 482–490.

Bishop, C., 1995. *Neural Networks For Pattern Recognition,* Oxford University Press.

Blackett, M. & Wooster, M.J., 2011. Evaluation of SWIR-based methods for quantifying active volcano radiant emissions using NASA EOS-ASTER data, *Geomatics, Nat. Hazards Risk,* **2,** 51–79.

Buongiorno, M.F. *et al.*, 1999. MVRRS Campaign: MIVIS mission on Sicilian volcanoes and ground measurements, *Quaderni di Geofisica, Pubblicazione N. 7, 1999,* editor: Istituto Nazionale di Geofisica.

Buongiorno, M.F., Realmuto, V.J. & Doumaz, F., 2002. Recovery of spectral emissivity from thermal infrared multispectral scanner imagery acquired over a mountainous terrain: a case study from Mount Etna Sicily, *Remote Sens. Environ.,* **79,** 123–133.

Calvari, S., Coltelli, M., Neri, M., Pompilio, M. & Scribano, V., 1994. The 1991–93 Etna eruption: chronology and lava flow field evolution, *Acta Vulcano.,* **4,** 1–14.

Carpenter, G.A., Gjaja, M.N., Gopal, S. & Woodcock, C.E., 1997. ART neural networks for remote sensing: vegetation classification from Landsat TM and terrain data, *IEEE T. Geosci. Remote Sens.,* **35,** 308–325.

Carpenter, G.A., Gopal, S., Macomber, S., Martens, S., Woodcock, C.E. & Franklin, J., 1999. A neural network method for efficient vegetation mapping, *Remote Sens. Environ.,* **70,** 326–338.

Chen, P.Y., Srinivasan, R., Fedosejevs, G. & Narasimhan, B., 2002. An automated cloud detection method for daily NOAA-14 AVHRR data for Texas, USA, *Int. J. Remote Sens.,* **23,** 2939–2950.

Cheng, B. & Titterington, D.M., 1994. Neural networks: a review from a statistical perspective, *Stat. Sci.,* **9**(1), 2–54.

Civco, D.L., 1993. Artificial neural networks for land-cover classification and mapping, *Int. J. Geogr. Inf. Syst.,* **7,** 173–186.

Colin, O., Rubio, M., Landart, P. & Mathot, E., 2007. VoMIR: over 300 volcanoes monitored in near real-time by AATSR, in *Proceedings of Envisat Symposium 2007,* Montreux, Switzerland, 23–27 April, 2007 (ESA SP-636, July 2007).

Crisp, J. & Baloga, S., 1990. A model for lava flows with two thermal componets, *J. geophys. Res.,* **95,** 1255–1270.

Davis, G., 2007, History of the NOAA satellite program, *J. Appl Remote Sens.,* **1,** 012504.

Devijver, P.A. & Kittler, J., 1982. *Pattern Recognition: A Statistical Approach,* Prentice-Hall.

Donegan, S. & Flynn, L.P., 2004. Comparison of the response of the Landsat 7 enhanced thematic mapper plus and the earth observing-1 advanced land imager over active lava flows, *J. Volc. Geotherm. Res.,* **135**(1–2), 105–126.

Dozier, J., 1981. A method for satellite identification of surface temperature fields of subpixel resolution, *Remote Sens. Environ.,* **11,** 221–229.

Dreyer, P., 1993. Classification of land cover using optimized neural nets on SPOT data, *Photogramm. Eng. and Rem. S.,* **59,** 617–621.

Duda, R.O. & Hart, P.E., 1973. *Pattern Classification and Scene Analysis,* John Wiley and Sons.

Fukunaga, K., 1990. *Introduction to Statistical Pattern Recognition,* 2nd edn, Academic Press.

Foody, G.M., 1995a. Land cover classification by an artificial neural network with ancillary information, *Int. J. Geogr. Inf. Syst.,* **1,** 527–542.

Foody, G.M., 1995b. Using prior knowledge in artificial neural network classification with a minimal training set, *Int. J. Remote Sens.,* **16,** 301–312.

Ganci, G., Vicari, A., Fortuna, L. & Del Negro, C., 2011. The HOTSAT volcano monitoring system based on combined use of SEVIRI and MODIS multispectral data, *Ann. Geophys.,* **54**(5), doi:10.4401/ag-5338.

Geman, S., Bienenstock, E. & Doursat, R., 1992. Neural networks and the bias variance dilemma, *Neural Comput.,* **4**(1), 1–58.

Hand, D.J., 1981. *Discrimination and Classification,* John Wiley and Sons.

Harris, A.J.L., Swabey, S.E.J. & Higgins, J., 1995. Automated thresholding of active lavas using AVHRR data, *Int. J. Remote Sens.,* **16**(18), 3681–3686.

Harris, A.J.L., Butterworth, A.L., Carlton, R.W., Downey, I., Miller, P., Navarro, P. & Rothery, D.A., 1997a. Low cost volcano surveillance from space: case studies from Etna, Krafla, Cerro Negro, Fogo, Lascar and Erebus, *B. Volcanol.,* **59,** 49–64.

Harris, A.J.L., Blake, S., Rothery, D.A. & Stevens, N.F., 1997b. A chronology of the 1991 to 1993 Mount Etna eruption using advanced very high resolution radiometer data: implications for real-time thermal volcano monitoring, *J. geophys. Res.,* **102,** 7985–8003.

Harris, A.J.L., Flynn, L.P., Keszthelyi, L., Mouginis-Mark, P.J., Rowland, S.K. & Resing, J.A., 1998. Calculation of lava effusion rates from Landsat TM data, B, *Vucanol.,* **60,** 52–71.

Harris, A.J.L., Flynn, L.P., Rothery, D.A., Oppenheimer, C. & Sherman, S.B., 1999. Mass flux measurements at active lava lakes: implications for magma recycling, *J. geophys. Res.,* **104**(B4), 7117–7136.

Harris, A.J.L., Murray, J.B., Aries, S.E., Davies, M.A., Flynn, L.P., Wooster, M.J., Wright, R. & Rothery, D.A., 2000a. Effusion rate trends at Etna and Krafta and their implications for eruptive mechanisms, *J. Vulcanol. Geotherm. Res.,* **102,** 237–269.

Harris, A.J.L. *et al.*, 2000b. Real-time Monitoring of Volcanic Hot Spots with Satellites, *Am. geophys. Un. Monogr. Series*, **116,** 139–159.

Harris, A.J.L., Pilger, E., Flynn, L.P., Garbeil, H., Mouginis-Mark, P.J., Kauahikaua, J. & Thornber, C., 2001. Automated, high temporal resolution, thermal analysis of Kilauea volcano, Hawaii, using GOES satellite data, *Int. J. Remote Sens.,* **22**(6), 945–967.

Harris, A.J.L., Pilger, E. & Flynn, L.P., 2002. Web-based hot spot monitoring using GOES: what it is and how it works, *Adv. Environ. Monitor. Model.,* **1**(3), 5–36.

Harris, A.J.L., Carniel, R. & Jones, J., 2005. Identification of variable convective regimes at Erta Ale lava lake, *J. Volc. Geotherm. Res.,* **142,** 207–223.

Hassoun, M.H., 1995. *Fundamentals of Artificial Neural Networks,* MIT Press.

Haykin, S., 1999. *Neural Networks. A Comprehensive Foundation,* Prentice Hall.

Hecht-Nielsen, R., 1990. *Neurocomputing,* Addison-Wesley.

Hewitson, B.C. & Crane, R.G., 1994. Looks and uses, in *Neural Nets: Applications in Geography,* pp. 1–9, eds Hewitson, B.C. & Crane, R.G., Kluwer.

Jadid, M.N. & Fairbairn, D.R., 1996. Predicting moment-curvature parameters from experimental data, *Eng. Appl. Artif. Intell.,* **9**(3), 309–319.

Kaminsky, E.J., Barad, H. & Brown, W., 1997. Textural neural network and version space classifiers for remote sensing, *Int. J. Remote Sens.,* **18,** 741–762.

Keramitsoglou, I., Sarimveis, H., Kiranoudis, C.T. & Sifakis, N., 2005. Radial basis function neural networks classification using very high spatial resolution satellite imagery: an application to the habitat area of Lake Kerkini (Greece), *Int. J. Remote Sens.,* **26,** 1861–1880.

Keszthelyi, L., Harris, A.J.L. & Dehn, J., 2003. Observations of the effect of wind on the cooling of active lava flows, *Geophys. Res. Lett.,* **30,** doi: 10.1029/2003GL017994. .

Kontoes, C.C., Raptis, V., Lautner, M. & Oberstadler, R., 2000. The potential of kernel classification techniques for land use mapping in urban areas using 5m-spatial resolution IRS-1C imagery, *Int. J. Remote Sens.,* **21,** 3145–3151.

Kurnaz, M.N., Dokur, Z. & Olmez, T., 2005. Segmentation of remote-sensing images by incremental neural network, *Pattern Recogn. Lett.,* **26,** 1096–1104.

Lek, S. & Guegan, J.F., 1999. Artificial neural networks as a tool in ecological modelling, an introduction, *Ecol. Model.,* **120,** 65–73.

Li, Z., Khananian, A., Fraser, R.H. & Cihlar, J., 2001. Automatic detection of fire smoke using artificial neural networks and threshold approaches applied to AVHRR imagery, *IEEE T. Geosci. Remote Sens.,* **39,** 1859–1870.

Lipman, P.W. & Banks, N.G., 1987. Aa flow dynamics, *Mauna Loa 1984. U.S.G.S,* professional Paper 1350, 1527–1567.

Lloyd, C.D., Berberoglu, S., Curran, P.J. & Atkinson, P.M., 2004. A comparison of texture measures for the per-field classification of Mediterranean land cover, *Int. J. Remote Sens.,* **25,** 3943–3965.

Lombardo, V. & Buongiorno, M.F., 2006. Lava flow thermal analysis using three infrared bands of remote sensing imagery: a study case from Mt.Etna 2001 eruption, *Remote Sens. Environ.,* **101**(2), 141–149.

Lombardo, V., Buongiorno, M.F., Merucci, L. & Pieri, D.C., 2004. Differences in Landsat TM derived lava flow thermal structure during summit and flank eruption at Mount Etna, *J. Volc. Geotherm. Res.,* **134**(1–2), 15–34.

Lombardo, V., Buongiorno, M.F. & Amici, S., 2006. Characterization of volcanic thermal anomalies by means of sub-pixel temperature distribution analysis, *B. Volcanol.,* **68**(07–08), 641–651.

Lombardo, V., Harris, A.J.L., Calvari, S. & Buongiorno, M.F., 2009. Spatial variations in lava flow field thermal structure and effusion rate derived from very high spatial resolution hyperspectral (MIVIS) data, *J. geophys. Res.,* **114,** B02208, doi:10.1029/2008JB005648.

Lombardo, V., Silvestri, M. & Spinetti, C., 2011. Near real time routine for volcano monitoring using infrared satellite data, *Ann. Geophys.,* **54**(5), doi:10.4401/ag-5336.

Marchese, F., Filizzola, C., Genzano, N., Mazzeo, G., Pergola, N. & Tramutoli, V., 2011. Assessment and improvement of a robust satellite technique (RST) for thermal monitoring of volcanoes, *Remote Sens. Environ.,* **115**(6), 1556–1563.

Mas, J.F., 2004. Mapping land use/cover in a tropical coastal area using satellite sensor data, GIS and artificial neural networks. Estuarine, *Coastal Shelf Sci.,* **59,** 219–230.

Masters, T., 1994. *Practical Neural Network Recipes in C++,* Academic Press.

Murai, H. & Omatu, S., 1997. Remote sensing image analysis using a neural network and knowledge-based processing, *Int. J. Remote Sens.,* **18,** 811–828.

Oppenheimer, C., 1991. Lava flow cooling estimated from Landsat Thematic Mapper infrared data: the Lonquimay eruption (Chile, 1989), *J. geophys. Res.,* **96,** 21 865–21 878.

Oppenheimer, C., 1993. Thermal distributions of hot volcanic surfaces constrained using three infrared bands of remote sensing data, *Geophys. Res. Lett.,* **20**(6), 431–434.

Oppenheimer, C., Rothery, D.A. & Francis, P.W., 1993a. Thermal distribution at fumarole fields: implications for infrared remote sensing of active volcanoes, *J. Volc. Geotherm. Res.,* **55,** 97–115.

Oppenheimer, C., Francis, P.W., Rothery, D.A., Carlton, R.W.T. & Glaze, L., 1993b. Infrared image analysis of volcanic thermal features: Làscar Volcano, Chile, 1984–1992, *J. geophys. Res.,* **98,** 4269–4286.

Paola, J.D. & Schowengerdt, R.A., 1995. A detailed comparison of backpropagation neural network and maximum-likelihood classifiers for urban land use classification, *IEEE T. Geosci. Remote Sens.,* **33,** 981–996.

Patrick, M., Dehn, J. & Dean, K., 2005. Numerical modeling of lava flow cooling applied to the 1997 Okmok eruption, II: comparison with AVHRR thermal imagery, *J. geophys. Res.,* **110,** B02210, doi:10.1029/2003JB002538.

Pergola, N., Marchese, F. & Tramutoli, V., 2004. Automated detection of thermal features of active volcanoes by means of Infrared AVHRR records, *Remote Sens. Environ.,* **93**(3), 311–327.

Pieri, D.C. & Baloga, S., 1986. Eruption rate, area and length relationships for some Hawaiian lava flows, *J. Volcanol. Geotherm. Res.,* **30,** 29–45.

Pieri, D.C., Glaze, L.S. & Abrams, M.J., 1990. Thermal radiance observation of an active lava flow during th June 1984 eruption of Mt. Etna, *Geology,* **18,** 1018–1022.

Prechelt, L., 1998. Automatic early stopping using cross validation: quantifying the criteria, *Neural Net.,* **11**(4), 761–767.

Qiu, F. & Jensen, J.R., 2004. Opening the black box of neural networks for remote sensing image classification, *Int. J. Remote Sens.,* **25,** 1749–1768.

Ripley, B.D., 1994. Neural networks and related methods for classification, *J. Roy. Stat. Soc. B,* **56**(3), 409–456.

Rosenblatt, R., 1962. *Principles of Neurodynamics,* Spartan Books.

Rothery, D.A., Francis, P.W. & Wood, C.A., 1988. Volcano monitoring using short wavelength infrared data from satellites, *J. geophys. Res.,* **93,** 7993–8008.

Rumelhart, D.E., Hinton, G.E. & Williams, R.J., 1986. Learning internal representations by error propagation, in *Parallel Distributed Processing: Explorations in the Microstructures of Cognition,* pp. 318–362, eds Rumelhart, D.E. & McClelland, J.L., MIT Press.

Rumelhart, D.E., Durbin, R., Golden, R. & Chauvin, Y., 1995. Backpropagation: the basic theory, in *Backpropagation: Theory, Architecture, and Applications,* pp. 1–34, eds Rumelhart, D.E. & Yves, C., Lawrence Erlbaum.

Schalkoff, R., 1992. *Pattern Recognition: Statistical, Structural and Neural Approaches,* Wiley.

Schalkoff, R.J., 1997. *Artificial Neural Networks,* McGraw-Hill.

Smithsonian Institution, Global Volcanism Program Digital Information Series, GVP-3, 2013. Available at: http://www.volcano.si.edu (last accessed 24 January 2013).

Spangenberg, D.A., Doelling, D.R., Chakrapani, V., Minnis, P. & Uttal, T., 2002. Nighttime cloud detection over the Arctic using AVHRR data, in *Proceedings of 12th ARM Science Team Meeting,* St. Petersburg, FL, April 8–12.

Steffke, A.M. & Harris, A.J.L., 2011. A review of algorithms for detecting volcanic hot spots in satellite infrared data, *B. Volcanol.,* **73,** 1109–1137.

Sunar, F. & Ozkan, C., 2001. Forest fire analysis with remote sensing data, *Int. J. Remote Sens.,* **22,** 2265–2277.

Tatem, A.J., Noor, A.M. & Hay, S.I., 2004. Defining approaches to settlement mapping for public health management in Kenya using medium spatial resolution satellite imagery, *Remote Sens. Environ.,* **93,** 42–52.

Wadge, G., 1977. The storage and release of magma on Mount Etna, *J. Volc. Geotherm. Res.,* **2,** 361–384.

Walker, G.P.L., 1973. Lengths of lava flows, *Philos. Trans. R. Soc. London,* **A274,** 107–118.

Wan, Z. & Dozier, J., 1989. Land-surface temperature measurement from space: physical principles and inverse modelling, *IEEE Trans. Geosci. Remote Sens.,* **27**(3), 268–277.

Webley, P.W. *et al.*, 2008. Experiences from near-real-time satellite based volcano monitoring in central America: case studies at Fuego, Guatemala, *Int. J. Remote Sens.,* **29,** 6621–6646.

Wooster, M.J. & Rothery, D.A., 1997. Time series analysis of effusive volcanic activity using the ERS along track scanning radiometer: the 1995 eruption of Fernandina volcano, Galapagos Island, *Remote Sens. Environ.,* **69,** 109–117.

Wright, R., Rothery, D.A., Blake, S. & Pieri, D.C., 2000. Improved remote sensing estimates of lava flow cooling: a case study of the 1991 to 1993 Mount Etna eruption, *J. geophys. Res.,* **105,** 23 681–23 694.

Wright, R., Blake, S., Harris, A. & Rothery, D., 2001. A simple explanation for the space-based calculation of lava eruptions rates, *Earth Planet. Sc. Lett.,* **192,** 223–233.

Wright, R., Flynn, L., Garbeil, H., Harris, A. & Pilger, E., 2004. MODVOLC: near-real-time thermal monitoring of global volcanism, *J. Volc. Geotherm. Res.,* **135,** 29–49.